Materials & Design 219 (2022) 110783

Contents lists available at ScienceDirect

Materials & Design

journal homepage: www.elsevier.com/locate/matdes

On the design of a piezoelectric self-sensing smart composite laminate

Maria Elena Gino [a,*], Giacomo Selleri [b], Davide Cocchi [c], Tommaso Maria Brugo [c], Nicola Testoni [b], Luca De Marchi [b], Andrea Zucchelli [c], Davide Fabiani [b], Maria Letizia Focarete [a]

[a] Department of Chemistry "Giacomo Ciamician" and INSTM UdR of Bologna, University of Bologna, via Selmi 2, 40126 Bologna, Italy
[b] Department of Electrical, Electronic, and Information Engineering, University of Bologna, Viale Risorgimento 2, 40136 Bologna, Italy
[c] Department of Industrial Engineering, University of Bologna, Viale Risorgimento 2, 40136 Bologna, Italy

HIGHLIGHTS

- A non-invasive method for piezoelectric functionalization of composite laminate by interleaving Lead Zirconate Titanate micro-powder is proposed.
- An analytical model based on the volumetric fractions is implemented to predict the piezoelectric behaviour of the self-sensing composite laminate.
- The proposed laminate functionalization does not impact on the strength of the hosting material, unlike conventional Structural Health Monitoring sensors.

GRAPHICAL ABSTRACT

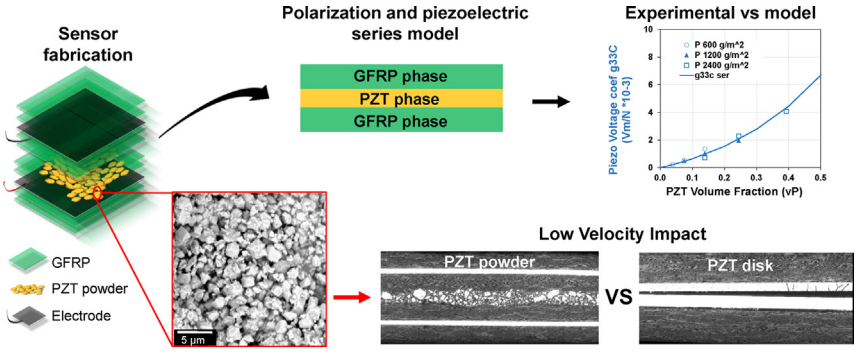

ARTICLE INFO

Article history:
Received 5 November 2021
Revised 23 May 2022
Accepted 23 May 2022
Available online 25 May 2022

Keywords:
Composites
Lead Zirconate Titanate (PZT)
Piezoelectrics
Sensing
Structural Health Monitoring (SHM)
Smart materials

ABSTRACT

The structural health monitoring of composite laminates is a rapidly emerging need in structural applications. Different real-time sensors integrated into laminates have been proposed, such as fiber Bragg gratings and piezoceramics. However, their presence negatively affects the mechanical properties of the hosting laminate.

This work proposes a non-invasive method for piezoelectric functionalization of composite laminates by interleaving lead zirconate titanate micrometric powder between glass-fiber-reinforced polymer plies. The effects of different powder volume fractions on the electromechanical properties were evaluated in terms of the electrical response and laminate inherent strength. The lead zirconate titanate powder laminates demonstrated an electrical sensitivity value that was up to 439% higher compared with that of the embedded commercial disk laminate (12.4 V/kN versus 2.3 V/kN). Impact tests revealed that the resistance of the interleaved lead zirconate titanate powder laminates is comparable to that of the pristine laminates, whereas a fragile commercial disk leads to delamination. Furthermore, an analytical model was proposed to predict the piezoelectric voltage coefficient g_{33} as a function of the electrical properties, volumetric powder fractions, and polarization process. The model matched the experimental g_{33} coefficients ($R^2 = 0.97$), demonstrating its capability to predict the electromechanical behavior of piezoelectric composites and define their design guidelines.

* Corresponding author.
E-mail address: mariaelena.gino2@unibo.it (M.E. Gino).

https://doi.org/10.1016/j.matdes.2022.110783
0264-1275/

1. Introduction

Fiber-reinforced plastics (FRP) are becoming a primary requirement in many engineering fields owing to their light weight, stiffness, and mechanical strength [1]. However, their laminar morphology presents a potentially critical issue because delamination can propagate between plies without any visual recognition of damage evolution. In this context, structural health monitoring (SHM) is an emerging technique for real-time supervision of the structural status and for accurate impact localization [2,3]. The sensors can be attached to the outer surface to avoid any alteration in the mechanical performance of the laminate; however, environmental conditions and external noise could affect their proper operation. Therefore, recent efforts have been made to embed sensors into composite laminates [4-6].

Broad investigations have been conducted on various types of sensors, such as strain gauges, optical fibers, capacitive sensors, and piezoelectric sensors [7]. Strain gauges, using a thin metallic grid, convert the laminate deformation into a resistance variation measured as a voltage change in the Wheatstone bridge circuit. Strain gauges are usually bonded to the component surface after the curing process and can be used to detect in-plane and bending deformations. Fiber Bragg grating (FBG) sensors embedded in the composite laminate convert the strain into a variation of the refractive index of the fiber core, causing a phase shift in the reflected wavelength [8]. However, the interleaving of an optical fiber between composite plies perpendicular to the reinforcing fiber direction constitutes a defect that can induce matrix cracking and subsequent delamination of the composite laminate [9]. Another sensing technique involves dispersing carbon nanotubes (CNTs) inside the host matrix to impart electrical conductivity [10]. As the structure is compressed, a correlation can be established between the mechanical deformation and measured electrical resistance. This type of piezoresistive composite material ensures proper quantification of the impact amplitude, but it does not provide damage localization. For this reason, ceramic piezoelectric materials such as lead zirconate titanate (PZT) are often preferred for elastic wave detection because they can be placed at strategic points in the composite material and identify the damaged region [11]. Saeedifar et al. validated a network composed of eight PZT wafers attached to a carbon-fiber-reinforced plastic (CFRP) composite plate surface for accurate damage localization [12]. Debonding of the structural components resulted in acoustic wave propagations that were successfully detected by the PZT disk attached to the CFRP plate surface [13]. PZT sensors can also be embedded into the composite laminate, which can more effectively localize damage [14] compared with sensors attached to the outer surfaces, as demonstrated by Yang et al. [15].

However, the brittle nature of the ceramic PZT material and bulky morphology of the disk can trigger delamination and dramatically decrease the strength of the hosting material [16,17]. The intrusiveness of the sensor in the hosting laminate can be reduced by changing the wafer morphology of the PZT to microfibers. For example, Konka et al. [18] found that the laminate shear strength could be reduced by 7% by embedding PZT microfibers in unidirectional GFRP prepreg plies compared with a 15% reduction by embedding a PZT disk. However, their dispersion in the matrix was hampered by difficult handling owing to their fragile nature and micrometric dimensions. Hwang et al. proposed an interleaving PZT in the form of a micrometric powder instead of a bulky disk for interleaving between GFRP plies [19]. This approach could be a viable strategy to functionalize the composite material, reducing the detrimental effect of fragile PZT on the inherent strength of the hosting laminate.

In this study, the epoxy matrix of the composite material was made piezoelectric by dispersing it inside the PZT powder. In particular, PZT powder was interleaved between the GFRP prepreg plies of the laminate together with thin brass sheets as electrodes to collect the piezoelectric signal. The effects of the PZT morphology (disk vs. powder) and PZT/GFRP volume ratio were analyzed in terms of the impact resistance of the hosting laminate and sensor performance.

A piezoelectric model was used to correlate the volumetric fraction of the two phases and the polarization process of the laminates with the electromechanical responses to impact.

2. Materials & methods

2.1. Fabrication process of the sensing laminate

All sensing laminates were fabricated using lead zirconate titanate (PZT) obtained from the commercial sensor Murata 7BB-35-3L0 composed of Piezotite® P-7B piezoelectric material (relative dielectric constant, ε_r = 1510; Curie temperature, T_c = 300 °C; piezoelectric strain coefficient, $d_{33} = 271 \times 10^{-12}$ m/V; and piezoelectric voltage coefficient $g_{33} = 20 \times 10^{-3}$ Vm/N, according to datasheet). The piezoelectric element was embedded in the composite in two different forms: a commercial sensor (COM), as obtained from the manufacturer; and PZT powder (PWD), which was obtained by grinding the PZT disk extracted from the commercial sensor. The manufacturing processes for the two types of piezoelectric laminates are shown in Fig. 1. In the COM laminate, the piezoelectric commercial sensor was embedded as is, and its electrodes (where the lower and upper electrodes were composed of a brass sheet and silver coating, respectively) and cables were used to collect the signal. For the PWD laminates, the PZT powder was extracted from the pristine sensor, as described in Section 2.1.1. Both the PZT disk and powder were embedded in the laminate following the procedure described in Section 2.1.2 and then poled according to Section 2.1.3. Finally, to acquire the piezoelectric signal, a circuit was designed, as described in Section 2.1.4.

2.1.1. Piezoelectric powder fabrication

To extract the piezoelectric element to produce the PZT powder, the PZT disk was separated from the pristine sensor via thermal treatment for 1 h at 350 °C (Fig. 1a–c). In this manner (i.e., by burning the adhesive), it was possible to easily detach the PZT disk from the commercial electrodes and disrupt the polarization by exceed-

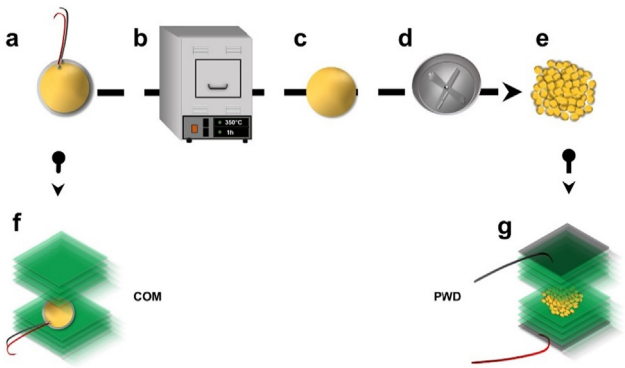

Fig. 1. Manufacturing process of the two types of piezoelectric laminates: (a) commercial sensor; (b) thermal treatment; (c) removal of electrodes; (d) PZT disk grinding into (e) powder; (f) COM laminate with the pristine sensor; and (g) PWD laminate with the PZT powder.

ing its Curie temperature (T_c) of 300 °C. The PZT powder was then obtained by grinding five PZT disks (equal to 16 g) in a single batch with a rotating blade mill (IKA A 10 basic) at 25 000 rpm for 20 s (Fig. 1d–e). In Fig. 2, scanning electron microscopy (SEM) images of the PZT powder morphology are shown at two different magnifications.

The PZT particle sizes were measured using image analysis software (ImageJ) on a sample of 100 particles. The PZT powder contains two different particle-dimension distributions: one with an average size of 24.6 ± 10.9 μm and another with 2.06 ± 0.26 μm.

2.1.2. Lamination and curing

To investigate the effect of the PZT morphology and PZT and GFRP volumetric fractions on the piezoelectric and mechanical properties of the hosting composite laminate, specimens with different stacking-sequence configurations were fabricated, as summarized in Fig. 3.

As a reference for the mechanical behavior, a pristine non-sensing laminate with 10 GFRP plies, labeled as REF-G10, was fabricated (Fig. 3a). A conventional sensing laminate, labeled COM, with eight GFRP plies and a commercial sensor interleaved in the laminate midplane was also fabricated (Fig. 3b). For the PWD laminates, a combination of three different PZT powder areal densities (600, 1200, and 2400 g/m^2) interleaved in the laminate midplane with three different numbers of GFRP plies (2, 4, and 8) between the electrodes was investigated (Fig. 3c). Note that the total number of GRFP plies in the PWD laminates was maintained as 8 by adding layers above and below the electrodes. For the reference REF-G10 laminate, 10 plies were stacked to obtain a thickness equal to or greater than that of the sensing laminates, compensating for the thickness of the piezoelectric elements and making all laminates mechanically comparable. In this exploratory study, only one specimen was manufactured for each configuration. All the specimens were composed of woven layers of GFRP prepreg (E-glass 8H Satin 300 g/m^2 epoxy matrix, VV300S - DT121H-34 Delta-Preg, 50 × 50 × 0.245 mm^3). For the PWD specimens, PZT powder was interleaved in the laminate midplane by depositing it on the GFRP prepreg before stacking. The powder was evenly dispersed using a customized vibrating dispersing tool and a circular mask with a diameter of 20 mm.

The partially cured prepreg resin (B-stage) was sufficient to impregnate the PZT powder without the need for additional resin. In the COM laminate (Fig. 3b), the electrodes of the commercial sensor were used to collect the piezoelectric signal, while for the PWD laminates (Fig. 3c), thin, circular brass sheets (∅ 20 × 0.1 m m^2 and ∅ 30 × 0.1 mm^2 for the top and bottom electrodes, respectively) were co-cured with the GFRP prepreg plies. Before stacking, the brass sheets were treated with sandpaper (P220), and signal cables with Teflon jackets were soldered onto them.

After stacking, all the laminates were cured in an autoclave by following a vacuum bag technique involving a optimized, three-step curing cycle, as described in ref. [20], to facilitate the impregnation of the PZT powder, evacuate air bubbles, and increase the glass transition temperature (T_g) of the epoxy resin to 132 °C.

2.1.3. Poling

Generally, to to obtain a material with a piezoelectric behavior, it is necessary to orient the dipoles through a poling process [21], where the poling temperature, poling time, and applied electric field typically depend on the electrical properties of the piezoelectric material. For PZT, the poling process is performed at a high temperature in order to increase the mobility of the dipoles during the application of a strong external electric field [22]. Simultaneously, the poling temperature of the composite materials should be maintained below the T_g of the polymeric matrix to avoid damaging the laminate. Indeed, above the T_g, the increased mobility of the macromolecules could lead to a rapid decrease in dielectric strength, causing electrical breakdowns [20]. Therefore, the temperature of the poling process was set to below the T_g of the epoxy resin. The PZT embedded in the laminates was poled by applying a DC electric field of 4 kV/mm across the two electrodes at 100 °C for 24 h. It was observed that electric fields higher than 4 kV/mm were unstable over a long period owing to electrical breakdown. In the end, the system was cooled to room temperature at 2 °C/min while the electric field was kept on.

2.1.4. Signal conditioning

As illustrated in the equivalent circuit of Fig. 4, the self-sensing laminate can be modeled as a charge generator q_p connected in parallel with its resistance and capacitance (R_s and C_s respectively), where R_s is generally sufficiently high so as to be omittable [23]. The electrical charges generated by the PZT are collected by the two brass electrodes and flow through the cables (C_c) to the amplifier resistance R_a, thereby generating a potential.

The measured cable capacitance was 5 pF, and according to the INA118 Texas Instruments supplier datasheet, the amplifier resistance was 10 GΩ. The signal was acquired using a National Instruments NI 9215 instrument.

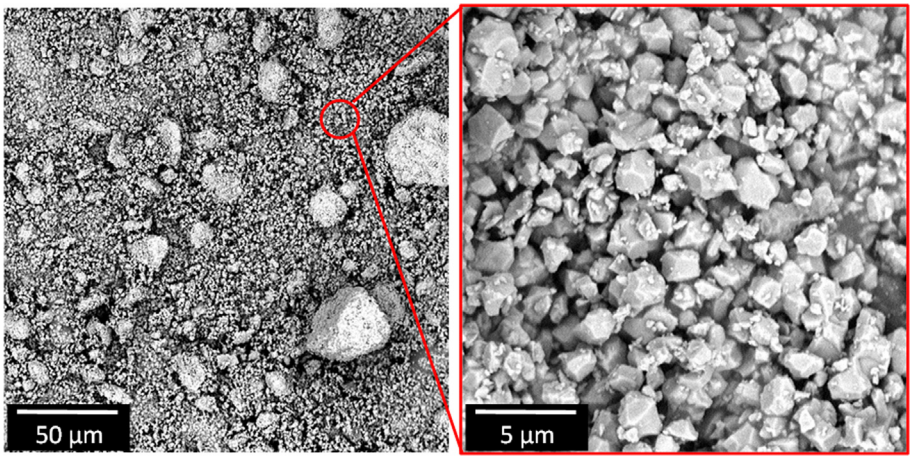

Fig. 2. SEM micrographs of PZT powder morphology at two different magnifications.

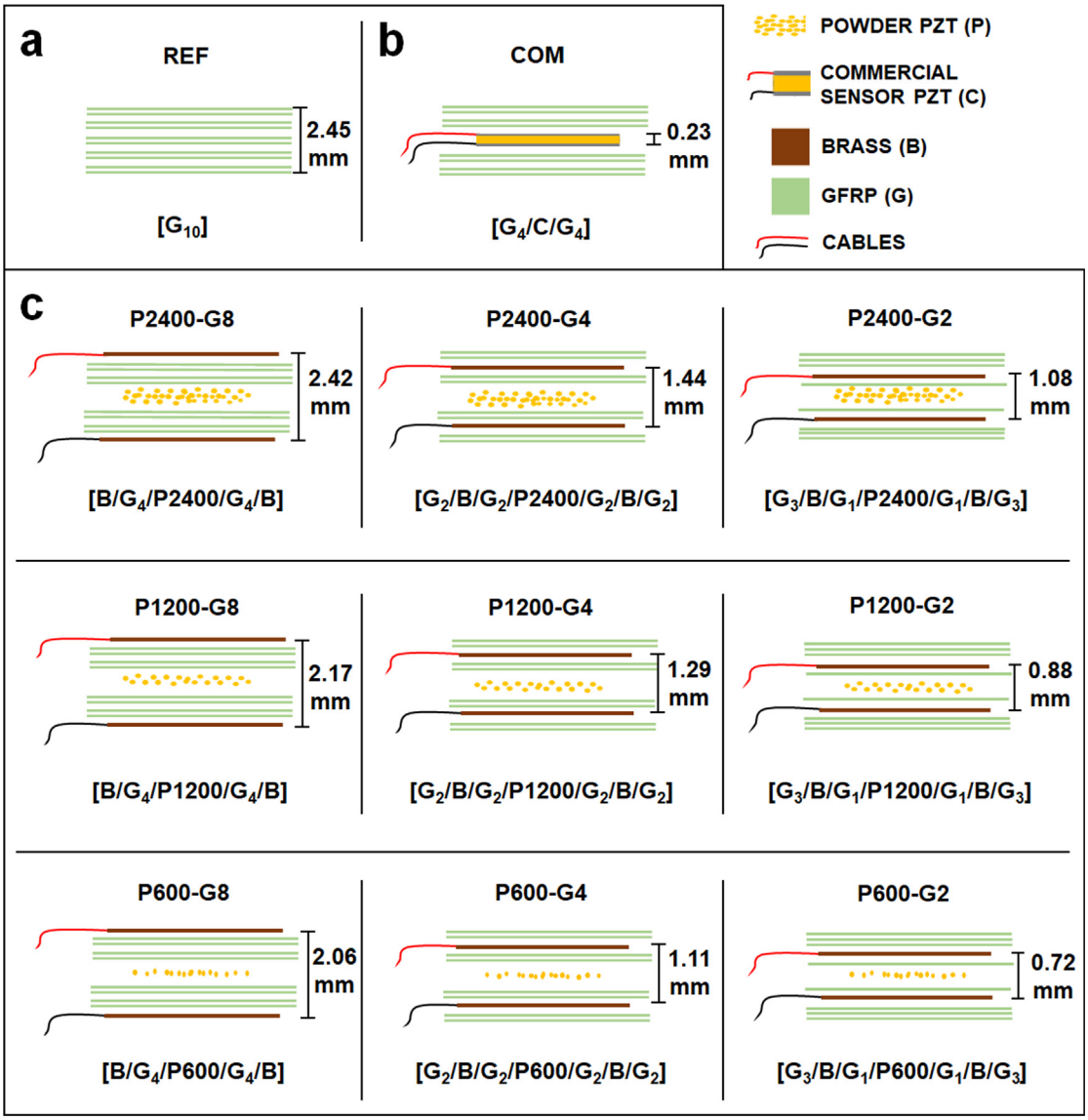

Fig. 3. Laminate stacking-sequence configurations: (a) non-sensing reference laminate, (b) laminate with embedded commercial sensor, (c) laminates with different PZT powder areal weights and number of GFRP plies between the electrodes.

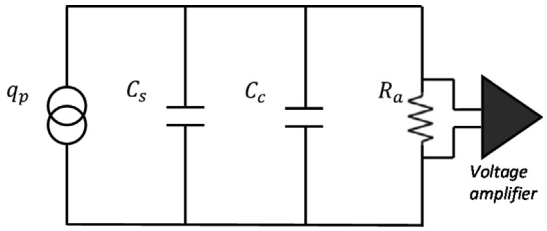

Fig. 4. Equivalent circuit of the piezoelectric laminate.

2.2. Electrical measurements

2.2.1. Phases electrical measurements

The conductivities of the single phases (GFRP and PZT) were measured using a picoammeter (Keysight B2981A). The dielectric constants of the single phases were measured using a dielectric analyzer (Novocontrol alpha dielectric analyzer B2.2) in the frequency range of 10^{-2}–10^{4} Hz.

The g_{33}^{p} of the PZT phase was evaluated for different poling electric-field intensities. The commercial disks were first treated in a muffle furnace to remove the initial polarization, as described in Section 2.1.1. Then, each disk was polarized in a dielectric silicon-oil bath at 100 °C (composite poling temperature) at different electric fields for 24 h, in the range of 0.1–3 kV/mm. Electric fields higher than 3 kV/mm resulted in electrical breakdown across the PZT disk.

2.2.2. Composite electrical measurements

The impedances of the sensing laminates were measured in the 40–400 kHz range using a precision impedance analyzer (Agilent 4294A). The capacitances were determined by interpolating the impedance vs. frequency curve using the linear equation of the RC circuit.

The piezoelectric responses of the sensing laminates were evaluated with a compressive cyclic load using an Instron 8033 hydraulic testing machine equipped with a 25 kN load cell. As shown in Fig. 5, the specimens were compressed between a flat plastic support and plastic cylindrical indenter with a diameter

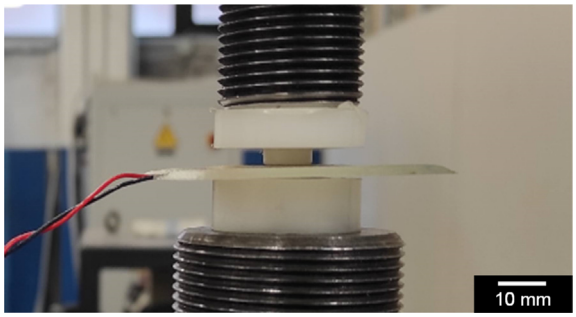

Fig. 5. Cyclic force indentation setup.

of 10 mm to electrically insulate the specimens. A compressive force oscillating between 0.5 and 1 kN at 25 Hz was applied; this frequency was chosen as the cyclic frequency was above the 3 dB cut-off frequency of the equivalent RC circuit represented in Fig. 4, allowing a non-attenuated and frequency-independent piezoelectric signal. Indeed, with a minimum equivalent capacitance ($C = C_s + C_c$) of 14.4 pF (according to the capacitance measurements reported in Section 3.2.2) and a resistance R_a of 10 GΩ, the estimated cut-off frequency was equal to 1.1 Hz. The force measured by the commercial load cell and the piezoelectric signal were acquired simultaneously at a frequency of 2 kHz.

Knowing the generated piezoelectric voltage as a function of the applied force, it is possible to determine the piezoelectric properties of a composite laminate by using two different coefficients that depend on its application. In the case of an actuator, the composite material can be described using the piezoelectric strain d_{33}^C (m/V) coefficient. On the other hand, for sensing applications, the composite material can be defined by the g_{33}^C (Vm/N) piezoelectric voltage coefficient, according to ref. [24,25].

Knowing the equivalent circuit parameters of the sensor and amplifier described in Fig. 4 as well as the voltage generated by the applied force F, it is possible to calculate the piezoelectric strain coefficient of the composite laminate, d_{33}^C. For a specific case of a sinusoidal load with angular frequency ω, according to ref. [23], the signal magnitude $|V|$ and phase shift φ for a piezoelectric sensor can be expressed as follows:

$$|V| = \frac{d_{33}^C F}{\sqrt{1 + \left(\frac{1}{\omega\tau}\right)^2 C}} \tan\varphi = \frac{1}{\omega\tau} \quad (1)$$

where $\tau = R_a C$ is the time constant.

For high $\omega\tau$ values, as in this case, Eq. (1) can be simplified as $|V| = F d_{33}^C / C$, and the d_{33}^C value can be simply calculated. Note that in this particular case, the output voltage is proportional to the applied load and is frequency-independent.

Finally, the g_{33}^C coefficient was calculated as the ratio of the d_{33}^C to the dielectric constant of the composite material ($g_{33}^C = d_{33}^C / \varepsilon_3^C$). By measuring the capacitance C, the electrode surface S, and the distance d of each composite laminate, the dielectric constant was derived as $\varepsilon_3^C = Cd/S$.

This procedure can be replicated for the calculation of the PZT-phase piezoelectric coefficients (i.e., d_{33}^P and g_{33}^P).

2.3. Low-velocity impact test

Low-velocity impact tests (LVI) were performed to investigate the effects of interleaving the piezoelectric element with different morphologies and PZT/GFRP weight ratios on the impact resistance of the hosting laminate. Tests were performed according to ASTM D7136 on a low-velocity impact machine with a 1.3 kg impactor mass equipped with a PCB 208C05 load cell and 12.7 mm hemispherical steel tip, as described in ref. [26] and shown in Fig. 6. Owing to the small dimensions of the specimen and to maximize the shear stress, a support plate containing a cylindrical hole with a diameter of 20 mm was used. The specimens were impacted at an energy of 3 J and a velocity of 2.2 m/s. An impact energy of 3 J was chosen so as to induce delamination without fiber breakage and to determine the effect of embedding an external body on the interlaminar strength of the laminate. Micrograph analyses of the cross-section of the laminates at the impact point were performed to evaluate the damaged zone.

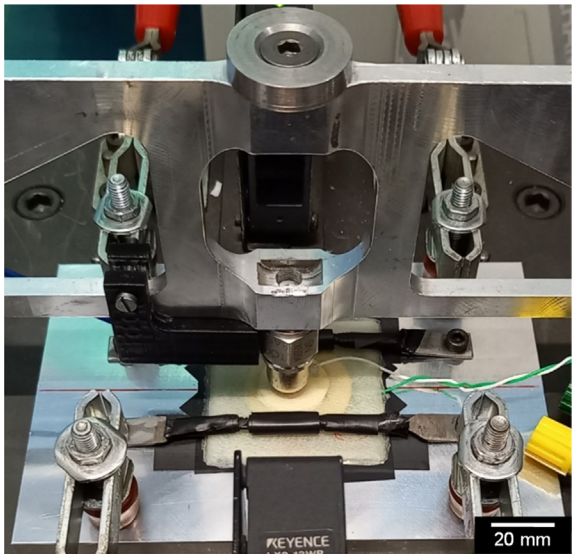

Fig. 6. Low-velocity impact setup.

3. Results and discussion

The experimentally measured electrical properties of the single-phase and composite configurations are reported in Section 3.1. In Section 3.2, the proposed polarization and piezoelectric models are described and validated using the aforementioned experimental data. Finally, the impact resistances of the sensing composite laminate configurations are compared in Section 3.3.

3.1. Electrical properties

3.1.1. Phase electrical properties

The absolute permittivity (ε), relative permittivity (ε_r), and conductivity (σ) of the single phases (PZT and GFRP), as reported in Table 1, were measured at 20 °C and 100 °C, which correspond to the working and polarization temperatures of the sensor, respectively. In particular, the permittivity values (ε^P and ε^G for PZT and GFRP, respectively) were determined for the regime state in the frequency domain, reached at 10^4 Hz, and the conductivity values (σ^P and σ^G for PZT and GFRP, respectively) were determined for the regime state, which was reached after 8 h.

Comparing the PZT and GFRP permittivity values, a difference of three orders of magnitude was observed at both temperatures. The conductivity difference between the two phases at 20 °C was two orders of magnitude, which decreased to one order of magnitude at 100 °C. This reduction of the conductivity gap between the two phases at 100 °C is crucial to the polarization process, as discussed in Section 3.2.1.

Table 1
Single-phase electrical properties.

	ε @ 20 °C (F/m 10^{-12})	ε @ 100 °C (F/m 10^{-12})	εr @ 20 °C	εr @ 100 °C	σ @ 20 °C (S/m 10^{-15})	σ @ 100 °C (S/m 10^{-15})
PZT	15,937	20,364	1801	2301	223	2600
GFRP	58	60	7	7	4	143

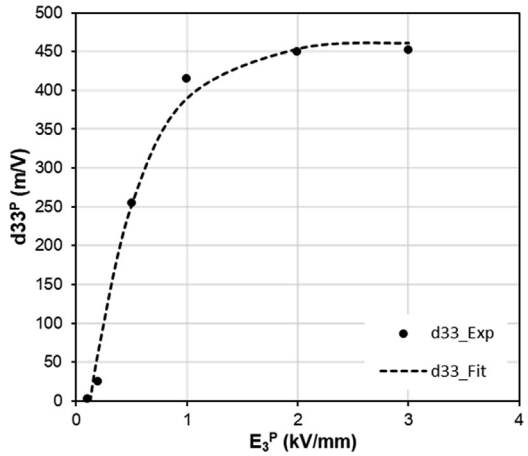

Fig. 7. PZT piezoelectric-strain-coefficient d_{33}^{P} vs. poling electric field E_3^P for 24 h at a temperature of 100 °C.

In Fig. 7, the experimentally measured d_{33}^{P} piezoelectric strain coefficients of the commercial PZT disks are plotted for the different electric-field magnitudes applied during the poling process, which was conducted at 100 °C for 24 h (represented by black dots). The d_{33}^{P} was measured using the same procedure as that for the self-sensing composite laminate, as described in Section 2.2.2. The experimental data were then interpolated using the exponential function given in Eq. (2) and employing the nonlinear least-squares method:

$$d_{33}^{P} = a * \left(1 - e^{bE_3^P}\right) - c \tag{2}$$

where the fitting coefficients a, b, and c are 614 pm/V, 2.19 mm/kV, and 143 pm/V, respectively. The interpolating equation is represented by the dotted line in the graph and has a coefficient of determination (R^2) of 0.985. As can be observed, the d_{33}^{P} rapidly increases with an increase in the electric field applied to PZT (E_3^P) and then stabilizes at 450 pm/V after 2 kV/mm.

3.1.2. Composite electrical properties

The measured capacitance values for each composite configuration are listed in Table 2. Generally, a drastic decrease in the composite capacitance occurs as the distance between the electrodes and the amount of GFRP plies (low dielectric constant) increases.

The piezoelectric sensitivity of the sensing laminates was evaluated using compressive cyclic loads, as described in Section 2.2.2. Overall, the piezoelectric responses of the samples accurately followed the applied force, as shown in Fig. 8 for samples P1200-G8, P1200-G4, and P1200-G2. Variations in the magnitude were registered, showing that the peak-to-peak piezoelectric output increased as the number of GFRP plies within the electrodes decreased.

In Fig. 9, the sensitivity is plotted as a function of the number of GFRP plies for all laminate configurations described in Fig. 3. The sensitivity of each laminate was calculated as the peak-to-peak ratio of the piezoelectric output to the applied force. A sensitivity value of 2.31 V/kN was measured for the commercial PZT sensor, as provided by the manufacturer and embedded in the composite laminate (COM). Generally, it can be observed that by integrating PZT in the form of powder (PWD) rather than the commercial PZT sensor, as provided by the manufacturer (COM), the sensitivity of the sensing laminate is sharply enhanced, especially for 1200 g/m^2 and 2400 g/m^2 PZT powder areal densities (yellow point vs. green and red curves). It is reasonable to assume that the physical mechanisms that enhance the piezoelectric performance of the PWD laminates stem from the microstructured shape of the PZT powder. The enhanced surface-to-volume ratio of the PZT powder with respect to the PZT bulk disk impacts both the mechanical and electrical properties of the laminate. First, compared with the COM laminate, the use of powder favors strain transmission from the GFRP matrix to the piezoelectric phase. Furthermore, the use of PZT powder results in a wider PZT area that faces the GFRP matrix, thus leading to an increase in the generated charges flowing toward the electrodes.

Considering the PWD laminates, by decreasing the number of GFRP plies interleaved between the electrodes, the sensitivity is considerably improved. Indeed, it can be reasonably assumed that the thickening of the insulating layer results in a reduction in the

Table 2
Experimental vs. model electrical parameters for each laminate configuration: volume fraction of PZT phase (v^P), equivalent capacitance for each laminate (C), absolute permittivity of the composite (ε_3^C), piezoelectric voltage coefficient of the composite (g_{33}^C), electric field applied to the PZT phase (E_3^P), and piezoelectric voltage coefficient of the PZT phase (g_{33}^P).

	Configuration				Experimental				Model		
	PZT (g/m^2)	n° GFRP within electrodes	d (mm) within electrodes	v^P	C (ρF 10^{-12})	ε_3^C (F/m10^{-12})	Sensitivity (mV/N)	g_{33}^C (Vm/N10^{-3})	E_3^P (kV/mm)	g_{33}^P (Vm/N10^{-3})	g_{33}^C (Vm/N10^{-3})
P2400-G8	2400	8	2.42	0.14	14.5	73	3.62	0.72	0.87	6.9	0.95
P2400-G4	2400	4	1.44	0.24	27.5	103	8.60	2.29	0.96	8.3	2.04
P2400-G2	2400	2	1.08	0.39	44.7	136	12.44	4.07	1.13	11.0	4.31
P1200-G8	1200	8	2.17	0.07	14.4	65	2.21	0.49	0.82	6.1	0.45
P1200-G4	1200	4	1.29	0.14	23.8	77	3.35	1.03	0.87	6.9	0.95
P1200-G2	1200	2	0.88	0.24	44.3	110	4.87	1.96	0.96	8.3	2.04
P600-G8	600	8	2.06	0.04	16.1	73	1.05	0.23	0.80	5.6	0.22
P600-G4	600	4	1.11	0.07	24.2	68	1.46	0.52	0.82	6.1	0.45
P600-G2	600	2	0.72	0.14	45.0	92	2.74	1.35	0.87	6.9	0.95

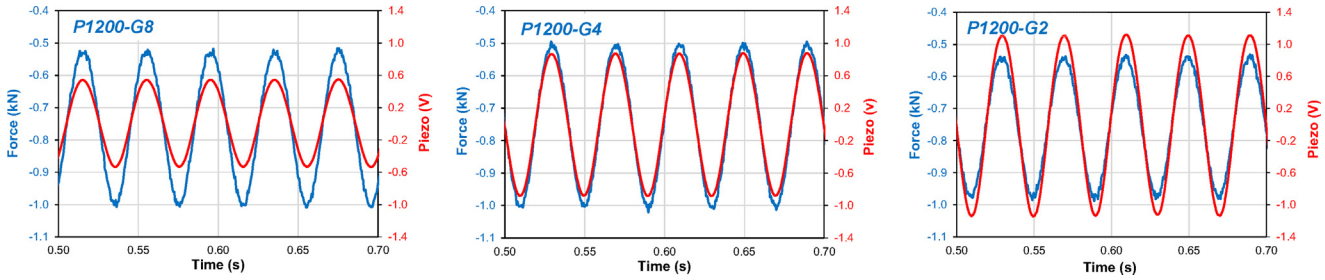

Fig. 8. Piezoelectric response of the sensing laminate (red curve) compared with the contact force measured by the indenter load cell (blue curve) for a powder sensor with 1200 g/m^2 and different plies of GFRP within the electrodes (8, 4, and 2, respectively). (For interpretation of the references to colour in this figure legend, the reader is referred to the web version of this article.)

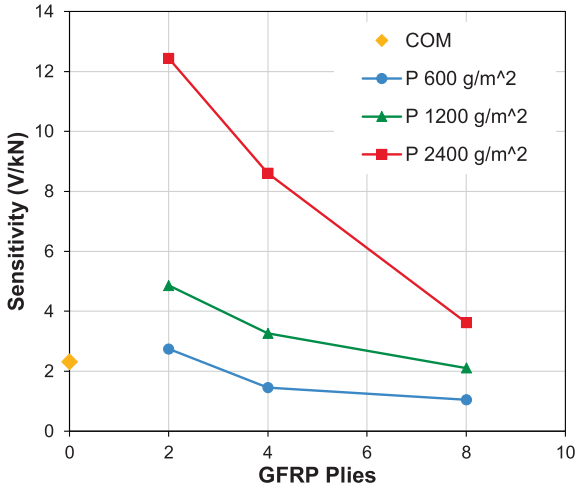

Fig. 9. Sensitivity vs. number of GFRP plies for commercial and powder-sensing laminates.

electric charges that reach the electrodes. Therefore, different numbers of GFRP plies (i.e., -G2, -G4, and -G8 laminate types) result in a change in the distance between the electrodes and a variation in the sensitivity of the laminates. Finally, for powder laminates, an exponential increase in the sensitivity as a function of the powder-to-resin weight ratio can be observed. This behavior is explained in detail in Section 3.2.2, considering model prediction.

Knowing the sensitivity values of the composite laminates, the experimental piezoelectric strain coefficients of the composites (g_{33}^{C}) can be calculated according to the procedure described in Section 2.2.2. These values are reported in Table 2 for each laminate configuration.

3.2. Polarization and piezoelectric composite model

To understand the piezoelectric behavior of the self-sensing laminate and to design it efficiently, it is necessary to consider the electrical and mechanical interactions between the two phases. By taking into account the cross-section of the self-sensing laminate (micrograph in Fig. 10a) and neglecting the transversal coupling, the piezoelectric composite can be modeled as a simple one-dimensional series connection between the two phases (Fig. 10b). First, a series-connected polarization model was developed to estimate the g_{33}^{P} of the piezoelectric phase, which depends on the effective electric field applied during the poling process (Section 3.2.1). Subsequently, a series-connected piezoelectric model was proposed to estimate the behavior of the laminate as

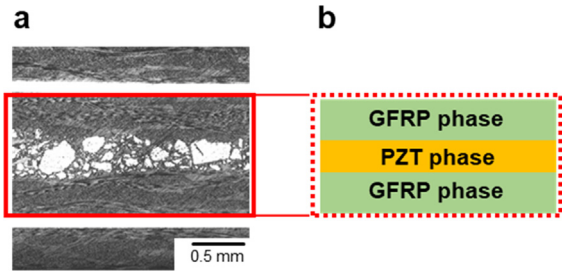

Fig. 10. (a) Micrograph and (b) equivalent series model of the self-sensing laminate.

both a sensor and actuator (Section 3.2.2) and was validated with previous experimental results.

3.2.1. Polarization model

As described in Section 2.1.3, all the fabricated piezoelectric composite laminates were polarized with an electric field of 4 kV/mm. However, unlike for bulk PZT materials, where the electric field is applied homogenously, the electric field was distributed unevenly between the PZT powder and GFRP phase [27].

The piezoelectric laminate can be modeled as a multilayered system in which the GFRP plies and PZT layer are connected in series, as schematically shown in Fig. 11, where each phase can be represented as a resistance (R^P, R^G) in parallel with a capacitance (C^P, C^G) [28].

By applying Kirchhoff's laws to the equivalent circuit according to ref. [27], the effective electric field applied to the piezoelectric phase can be calculated as follows:

$$E_3^P(t) = E_{3_{SS}}^P + (E_{3\_TR}^P - E_{3\_SS}^P)e^{-t/\tau} \tag{3}$$

$$E_{3\_SS}^P = \frac{\frac{E_3^C}{\sigma^P}}{\frac{v^P}{\sigma^P} + \frac{1-v^P}{\sigma^G}}, E_{3\_TR}^P = \frac{E_3^C\,\varepsilon^G}{\frac{v^P}{\varepsilon^G} + \frac{1-v^P}{\varepsilon^P}} \tag{4}$$

$$\tau = \tau^G * \tau^P \frac{\frac{1}{\varepsilon^P} + \frac{1-v^P}{v^P\varepsilon^G}}{\frac{1}{\sigma^P} + \frac{1-v^P}{v^P\sigma^G}} \tag{5}$$

where E_3^C is the electric field applied to the composite laminate (4 kV/mm); $E_{3\_SS}^P$ and $E_{3\_TR}^P$ are the steady-state and transient-state electric fields applied to the PZT phase, respectively; ε, σ, and v are the dielectric constant, conductivity, and volumetric fraction, respectively; the superscripts P and G refer to the PZT and GFRP phases, respectively; t is the time of application of the electric field; and τ is the time constant representing the time needed to reach 63% of the regime value, according to Eq. (3).

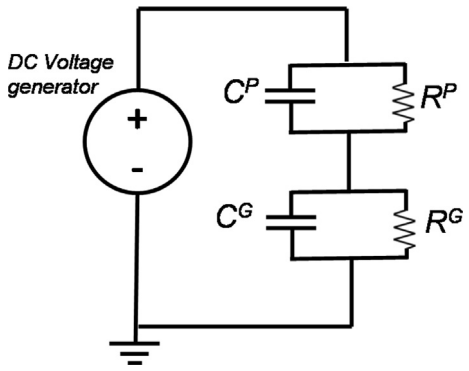

Fig. 11. Polarization-lumped model of the piezoelectric composite, where the PZT (P subscript) and GFRP (G subscript) phases are modeled as a capacitance and a resistor in parallel.

As shown in the graph in Fig. 12, when the DC voltage generator is switched on, the first transient domain distributes the electric field ($E^P_{3\_TR}$) on the phases according to their permittivity (ε^G and ε^P). After a period τ, the steady state is reached, and the electric field distribution ($E^P_{3\_SS}$) on the two phases is governed by the electrical conductivity (σ^G and σ^P) of the materials [29]. The electric field distributions of the two dielectric materials were evaluated as described in ref. [30]. The electric field strength reached in the steady-state regime and the transient period τ for the PZT and GFRP composites depended on the volumetric fraction of the two phases (v^P, v^G). In particular, by increasing v^P, the electric field applied to the PZT phase increased, and the time constant τ decreased. However, the τ value was still on the order of several hours for all the laminates, as calculated using Eq. (5) based on the electrical properties of the single constituents.

In this study, a poling time of 24 h was chosen to reach the steady-state regime of the electric field distribution in the PZT phase; therefore, Eq. (3) can be simplified to $E^P_3 = E^P_{3\_SS}$, according to the asymptotic behavior observed in the graph shown in Fig. 12. The piezoelectric strain coefficient of the PZT phase (d^P_{33}), obtained during the polarization of the self-sensing laminate, can then be estimated by substituting E^P_3 into Eq. (2), and the g^P_{33} can be derived as the ratio of d^P_{33} to ε^P. The calculated E^P_3 and g^P_{33} values are reported in Table 2 for each laminate configuration.

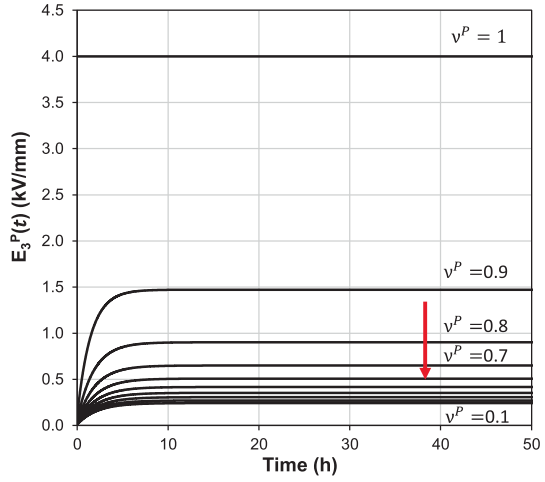

Fig. 12. Electric field applied to the PZT phase (E^P_3) of the composite as a function of its volumetric fraction (v^P) and time.

3.2.2. Piezoelectric model

When the piezoelectric composite was mechanically loaded, the electric charges generated by the PZT piezoelectric phase flowed toward the electrodes passing through the GFRP plies. The presence of the dielectric GFRP phase influenced the piezoelectric response of the self-sensing laminate, as can be observed in the graph in Fig. 9.

The piezoelectric behavior of the laminate can be described as a simple one-dimensional series-connected model of the two phases, as shown in Fig. 10. Subsequently, according to refs. [24] and [25], by applying the electric and mechanical boundary conditions to the direct and indirect constitutive piezoelectric equations, the equations for the composite piezoelectric strain (d^C_{33}) and voltage (g^C_{33}) coefficients can be obtained for the series-connected model:

$$d^C_{33} = \frac{v^P d^P_{33} \varepsilon^G + v^G d^G_{33} \varepsilon^P}{v^P \varepsilon^G + v^G \varepsilon^P} \tag{6}$$

$$g^C_{33} = v^P g^P_{33} + v^G g^G_{33} \tag{7}$$

where d^P_{33} and d^G_{33} are the piezoelectric strain coefficients of the PZT and GFRP phases, respectively, and g^P_{33} and g^G_{33} are the piezoelectric voltage coefficients of the PZT and GFRP phases, respectively. Equations (6) and (7) can be simplified by assuming that the piezoelectric strain and voltage coefficient of the GFRP phases are null.

Therefore, by substituting into Eq. (6) the piezoelectric strain coefficient of the PZT phase, d^P_{33}, which was determined using the polarization model described in Section 3.2.1 and the dielectric properties of the single phases, it is possible to calculate the piezoelectric strain coefficient of the composite, d^C_{33}. Similarly, Eq. (7) can be used to calculate the piezoelectric voltage coefficient of the composite, g^C_{33}.

The calculated trend of g^C_{33} as a function of the volumetric fraction of the piezoelectric phase (v^P) is reported in Fig. 13 (blue curve) and compared with the experimental data for the P600, P1200, and P2400 laminate configurations (blue dots). A parabolic trend was observed for the model that predicted the experimental g^C_{33} values, with $R^2 = 0.967$. The sharp increase in g^C_{33} as a function of the volumetric fraction correlated with two main physical factors. According to Eq. (7), the g^C_{33} of the composite is linearly dependent on the volumetric fraction of the piezoelectric phase (g^G_{33} = 0). Therefore, if g^P_{33} is constant, g^C_{33} is linearly proportional to the amount of the piezoelectric phase. However, the piezoelectric coefficient g^P_{33} depends on the polarization electric field applied to the PZT once it is integrated into the composite. This electric field ($E^P_{3\_SS}$), under stationary conditions, depends on the electrical conductivities of the individual phases and their volumetric fractions, in accordance with Eq. (4). Considering that the conductivity of the piezoelectric phase is one order of magnitude greater than that of the GFRP phase, the higher the volumetric fraction of the piezoelectric phase, the higher the amplitude of the electric field. Consequently, the value of g^P_{33}, obtained during polarization (see Section 3.1.1), increased as the volume fraction of the PZT increased. Therefore, adopting Eq. (7), g^C_{33} depends on v^P and on g^P_{33}, which in turn depends on v^P. Hence, this double dependence on v^P results in a parabolic trend in the g^C_{33} curve.

On the other hand, it can be observed that the piezoelectric strain coefficient of the composite, d^C_{33}, rapidly decreases for small amounts of the GFRP phase. For v^P = 0.9, the d^C_{33} of the composite dropped to 3% of the d^P_{33} value for the pure PZT. These results suggest that the composite laminate can be used for sensing applications with a wide range of PZT volumetric fractions (v^P), whereas

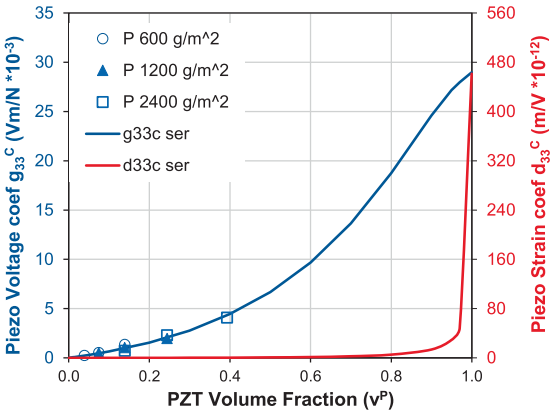

Fig. 13. Composite piezoelectric voltage coefficient g_{33}^{C} (blue curve) and strain coefficent d_{33}^{C} (red curve) vs. PZT volume fraction v^{P}, as estimated by the model. The blue dots represent the g_{33}^{C} experimental data measured for P600, P1200, and P2400 laminates. (For interpretation of the references to colour in this figure legend, the reader is referred to the web version of this article.)

high and unfeasible v^{P} values are necessary for actuator applications.

3.3. Impact resistance

The effect of embedding the piezoelectric PZT with different morphologies and quantities on the impact resistance of the hosting material was evaluated by low-velocity impact experiments following the procedure described in Section 2.3. In Fig. 14, the impact contact force vs. displacement responses for the different laminate types are plotted.

As shown in Fig. 14a, the curve of the laminate embedded with the commercial sensor (COM) contains multiple load drops, which are correlated with the breakages of the fragile ceramic disk. However, the absorbed energy was slightly lower than that of the reference laminate (REF-G10) because the breakage of the PZT ceramic disk absorbed a low amount of energy. For the PZT-powder-interleaved laminates, represented in Fig. 14b–d, the force vs. displacement curves do not show significant load drops linked to breakages.

To directly assess the impact behavior of the laminates, a micrograph analysis of the cross-section at the impact point was performed. The most significant samples are displayed in Fig. 15, where only half of the micrographs are shown, as the damage was symmetric with respect to the impact axis.

The reference laminate contained a few small 45°-oriented matrix cracks that propagated as a minor delamination between the GFRP layers along the midplane.

Conversely, for the commercial PZT sensor embedded in the composite (COM), the lower brass electrode was completely debonded from the PZT disk and adjacent GFRP ply. Moreover, the PZT disk exhibited multiple 45°-oriented cracks. Indeed, the bulky and fragile ceramic disk integrated into the laminate cracks and triggered delamination owing to the stiffness mismatch between the PZT and GFRP layers.

In the powder laminate P1200-G8, debonding of the external electrodes occurs, except in the case where the electrodes are interleaved inside the laminate (e.g., P1200-G4 and P1200-G2), where the bending stress is lower. The P1200-G8 specimen did not display cracks corresponding to the midplane where the PZT powder was interleaved, while P1200-G4 and P1200-G2 presented a remarkable 45° crack propagating in a reverse pine-tree pattern induced by the high Hertzian contact stress [31]. This crack continued to propagate as delamination occurred between the GFRP plies and PZT phase. The lower impact resistance of the P1200-G2 laminate can be ascribed to the high amount of PZT powder compared to the epoxy resin of the GFRP prepreg. Indeed, all the specimens with 600 g/m^2 PZT powder showed negligible cracks and delamination through the PZT layer (in Fig. 15, specimen P600-G4 is shown as a representative example), while all the specimens with 2400 g/m^2 PZT powder showed remarkable cracks propagating through the PZT layer (see P2400-G4, for example).

The qualitative analyses of Figs. 14 and 15 were performed using the measurements of the absorbed energy and delamination length for each laminate, respectively, as shown in the bar graph in Fig. 16.

The absorbed energy of the powder laminates (blue columns in Fig. 16) was generally slightly higher than the reference value. The energy dissipated during impact is generally linked to viscous damping and laminate damage, such as fiber breakage and plasticization [31], which are high-energy absorption mechanisms. In this particular case, the ductile brass electrodes are likely to plasticize during impact and absorb energy, especially if positioned in the outer layers of the G8 configuration, where the bending stress is higher. However, owing to the absorbed energy, it is difficult to detect matrix cracks and delamination because they are low-energy absorbing events. For this reason, the delamination length measurements of the micrograph analysis are shown in the bar graph in Fig. 16 (red columns). The total delamination was measured as the sum of the lengths of the matrix longitudinal delamination, electrode debonding from the GFRP ply, and the 45°-oriented cracks.

Owing to its bulky morphology, the COM is the most damaged laminate. Among the PWD laminates, the highest values of delamination length were observed for the G8 laminates, regardless of the PZT areal density. As mentioned previously, the external disposition of the electrodes leads to remarkable debonding at the interface with the GFRP ply. In the case of the G2 laminates, the interleaving of the electrodes between the GFRP plies improves the impact resistance; however, considerable delamination is still observed in the red columns of Fig. 16. Instead, delamination is lower for the P600-, P1200-, and P2400-G4 samples. Generally, by increasing the PZT amount or reducing the number of GFRP

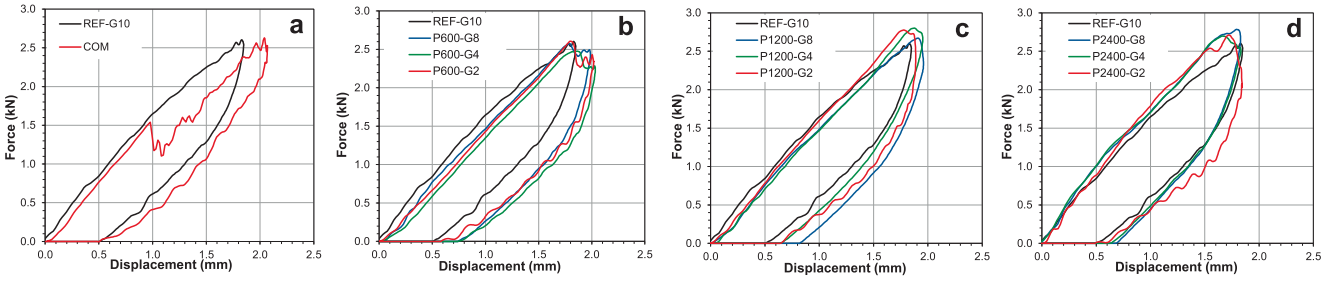

Fig. 14. Low-velocity impact test at 3 J: impact contact force vs. displacement response.

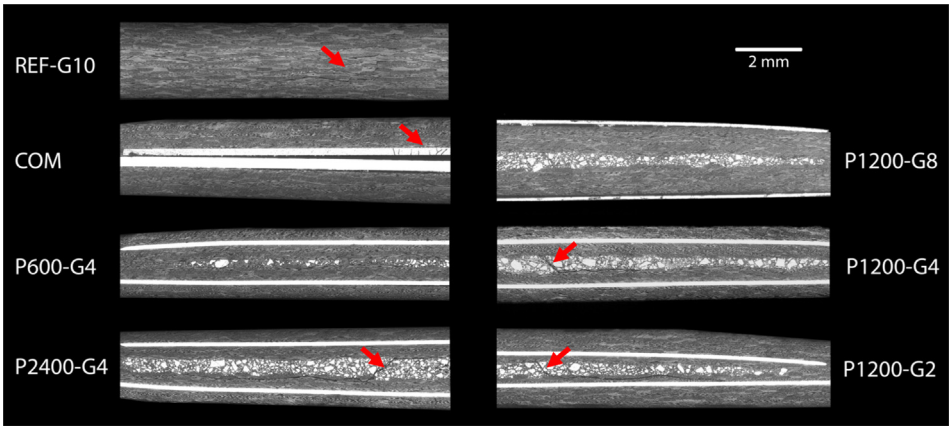

Fig. 15. Micrograph analysis of the cross-section of the laminates at the impact point. The red arrows indicate cracks. (For interpretation of the references to colour in this figure legend, the reader is referred to the web version of this article.)

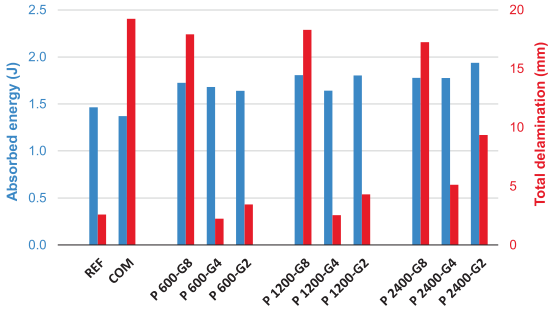

Fig. 16. Absorbed energy for low-velocity impact test at 3 J (blue columns) and total delamination length (red columns). (For interpretation of the references to colour in this figure legend, the reader is referred to the web version of this article.)

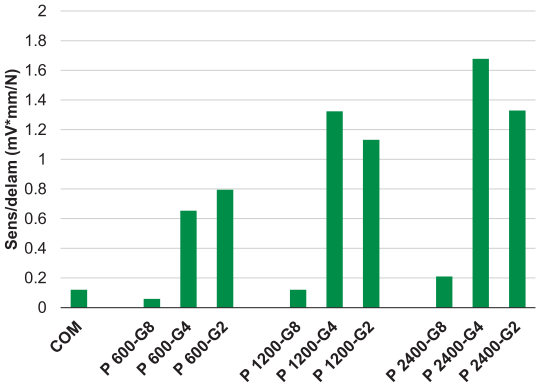

Fig. 17. Figures of merit of the self-sensing laminates, considering the ratio between the sensitivity and measured delamination length.

plies between the electrodes, the delamination total length increases owing to the lower ratio between the epoxy resin of the GFRP plies and PZT powder.

Finally, a figure of merit representing the ratio between the sensitivity (mV/N) and delamination length (mm) is shown in Fig. 17. Among the PWD laminates, the coefficient of merit exhibits an increasing trend for higher PZT amounts. P2400-G4 presented the highest coefficient of merit, but the value of total delamination was higher than the reference value. Therefore, P1200-G4 is the best compromise, as it has a self-sensing capability and impact resistance most comparable to those of the reference laminate.

4. Conclusions

In this study, a piezoelectric self-sensing composite material was successfully fabricated using ceramic PZT powders. The piezoelectric powder was interleaved between the GFRP prepreg plies, and brass-sheet electrodes were used to collect the piezoelectric signals. The effect of the PZT powder volume fraction on the electromechanical properties was investigated experimentally, and the results were compared with those of a piezoelectric laminate prepared using a PZT commercial disk. The PZT powder laminates show a higher sensitivity compared with that of the PZT commercial disk laminate (e.g., 12.44 V/kN for P2400-G2 vs. 2.31 V/kN for COM).

To understand the piezoelectric behavior and design guidelines for the fabrication of the self-sensing laminate, an analytical series-connected model was proposed. Based on the electrical properties of the two phases (GFRP and PZT), their volumetric fractions, and the polarization process, the model can predict the piezoelectric response of the laminate and effectively assist in its design. The model fitted the experimental results with a coefficient of determination of 0.97. Moreover, it allowed the prediction of the piezoelectric composite as an actuator, showing that even for a low volumetric fraction of GFRP, the piezoelectric strain coefficient d_{33} drastically decreases, confirming its impracticality as an actuator. The model can be adapted for the general design of piezoelectric-composite smart materials with embedded piezoelectric phases comprising different materials (e.g., PVDF) and morphology (e.g., nanofibers).

With respect to the mechanical performance, the micrometric powder dispersion slightly affected the impact resistance of the hosting composite laminate, whereas the embedded, fragile PZT commercial sensor dramatically triggered delamination. Based on the designed application, figures of merit were determined to identify the composite representing the best compromise between impact resistance and sensing capability. In particular, the P1200-G4 PZT powder laminate showed impact damage comparable to that of the non-sensing reference counterpart and a sensitivity 45% higher than that of the embedded COM.

CRediT authorship contribution statement

Maria Elena Gino: Conceptualization, Methodology, Investigation, Formal analysis, Writing – original draft. **Giacomo Selleri:** Conceptualization, Methodology, Investigation, Formal analysis, Writing – original draft. **Davide Cocchi:** Conceptualization, Methodology, Investigation, Formal analysis, Writing – original

draft. **Tommaso Maria Brugo:** Conceptualization, Methodology, Investigation, Formal analysis, Writing – original draft. **Nicola Testoni:** Investigation, Conceptualization. **Luca De Marchi:** Investigation, Conceptualization. **Andrea Zucchelli:** Conceptualization, Supervision. **Davide Fabiani:** Conceptualization, Supervision. **Maria Letizia Focarete:** Conceptualization, Supervision.

Data availability

The processed data required to reproduce these findings can be downloaded from [https://data.mendeley.com/datasets/4h3c-n476jv/1].

Declaration of Competing Interest

The authors declare that they have no known competing financial interests or personal relationships that could have appeared to influence the work reported in this paper.

Acknowledgments

This research was funded by the European Union's Horizon 2020 Research and Innovation Programme – "MyLeg" (No. 780871, 2018). The authors also wish to acknowledge the project POR-FESR 2018 - "i-LBBox (Intelligent Lightweigth Battery Box)" (No. E31B19000230009) for their financial support.

References

[1] M. Bazli, H. Ashrafi, A. Jafari, X.L. Zhao, R.K. Singh Raman, Y. Bai, Effect of fibers configuration and thickness on tensile behavior of GFRP laminates exposed to harsh environment, Polymers (Basel) 11 (9) (2019) 1–23, https://doi.org/10.3390/polym11091401.

[2] P.T. Coverley, W.J. Staszewski, Impact damage location in composite structures using optimized sensor triangulation procedure, Smart Mater. Struct. 12 (5) (2003) 795–803, https://doi.org/10.1088/0964-1726/12/5/017.

[3] S. Rana, P. Subramani, R. Fangueiro, A.G. Correia, A review on smart self-sensing composite materials for civil engineering applications, AIMS Mater. Sci. 3 (2) (2016) 357–379, https://doi.org/10.3934/matersci.2016.2.357.

[4] P. Hofmann, A. Walch, A. Dinkelmann, S. K. Selvarayan, and G. T. Gresser, "Woven piezoelectric sensors as part of the textile reinforcement of fiber reinforced plastics," *Compos. Part A Appl. Sci. Manuf.*, vol. 116, no. October 2018, pp. 79–86, 2019, doi: 10.1016/j.compositesa.2018.10.019.

[5] J. Cai, L. Qiu, S. Yuan, L. Shi, PeiPei Liu, D. Liang, Structural Health Monitoring for Composite Materials, in: N. Hu (Ed.), Composites and Their Applications, InTech, 2012.

[6] Y. Meyer, R. Lachat, G. Akhras, A review of manufacturing techniques of smart composite structures with embedded bulk piezoelectric transducers, Smart Mater. Struct. 28 (5) (2019) 053001.

[7] U. Pierre Claver, G. Zhao, Recent Progress in Flexible Pressure Sensors Based Electronic Skin, Adv. Eng. Mater. 23 (5) (2021) 1–17, https://doi.org/10.1002/adem.202001187.

[8] C. Sonnenfeld, G. Luyckx, S. Sulejmani, T. Geernaert, S. Eve, M. Gomina, K. Chah, P. Mergo, W. Urbanczyk, H. Thienpont, J. Degrieck, F. Berghmans, Microstructured optical fiber Bragg grating as an internal three-dimensional strain sensor for composite laminates, Smart Mater. Struct. 24 (5) (2015) 055003.

[9] K. Shivakumar, A. Bhargava, Failure mechanics of a composite laminate embedded with a fiber optic sensor, J. Compos. Mater. 39 (9) (2005) 777–798, https://doi.org/10.1177/0021998305048156.

[10] J. Qiu, X. Guo, R. Chu, S. Wang, W. Zeng, L. Qu, Y. Zhao, F. Yan, G. Xing, Rapid-Response, Low Detection Limit, and High-Sensitivity Capacitive Flexible Tactile Sensor Based on Three-Dimensional Porous Dielectric Layer for Wearable Electronic Skin, ACS Appl. Mater. Interfaces 11 (43) (2019) 40716–40725.

[11] A. Huijer, C. Kassapoglou, and L. Pahlavan, "Acoustic emission monitoring of carbon fibre reinforced composites with embedded sensors for in-situ damage identification," *Sensors*, vol. 21, no. 20, 2021, doi: 10.3390/s21206926.

[12] M. Saeedifar, J. Mansvelder, R. Mohammadi, D. Zarouchas, Using passive and active acoustic methods for impact damage assessment of composite structures, Compos. Struct. vol. 226, no. July (2019), https://doi.org/10.1016/j.compstruct.2019.111252 111252.

[13] J. Jiang, J. Jiang, X. Deng, and Z. Deng, "Detecting debonding between steel beam and reinforcing CFRP plate using active sensing with removable PZT-based transducers," *Sensors (Switzerland)*, vol. 20, no. 1, 2020, doi: 10.3390/s20010041.

[14] C. Tuloup, W. Harizi, Z. Aboura, Y. Meyer, Structural health monitoring of polymer-matrix composite using embedded piezoelectric ceramic transducers during several four-points bending tests, Smart Mater. Struct. 29 (12) (2020) 125011.

[15] B. Yang, F.-Z. Xuan, P. Jin, C. Hu, B. Xiao, D. Li, Y. Xiang, H. Lei, Damage Localization in Composite Laminates by Building in PZT Wafer Transducers: A Comparative Study with Surface-Bonded PZT Strategy, Adv. Eng. Mater. 21 (3) (2019) 1801040.

[16] S. Butler, M. Gurvich, A. Ghoshal, G. Welsh, P. Attridge, H. Winston, M. Urban, N. Bordick, Effect of embedded sensors on interlaminar damage in composite structures, J. Intell. Mater. Syst. Struct. 22 (16) (2011) 1857–1868.

[17] C. Tuloup, W. Harizi, Z. Aboura, Y. Meyer, Integration of piezoelectric transducers (PZT and PVDF) within polymer-matrix composites for structural health monitoring applications: new success and challenges, Int. J. Smart Nano Mater. 11 (4) (2020) 343–369, https://doi.org/10.1080/19475411.2020.1830196.

[18] H.P. Konka, M.A. Wahab, K. Lian, The effects of embedded piezoelectric fiber composite sensors on the structural integrity of glass-fiber–epoxy composite laminate, Smart Mater. Struct. 21 (1) (2012) 015016.

[19] M.Y. Hwang, L.H. Kang, Characteristics and fabrication of piezoelectric GFRP using smart resin prepreg for detecting impact signals, Compos. Sci. Technol. 167 (July) (2018) 224–233, https://doi.org/10.1016/j.compscitech.2018.08.002.

[20] T.M. Brugo, E. Maccaferri, D. Cocchi, L. Mazzocchetti, L. Giorgini, D. Fabiani, A. Zucchelli, Self-sensing hybrid composite laminate by piezoelectric nanofibers interleaving, Compos. Part B Eng. 212 (2021) 108673.

[21] R.G. Kepler, R.A. Anderson, Ferroeletric polymers, Adv. Phys. 41 (1) (1992) 1–57.

[22] G. Eberle, E. Bihler, W. Eisenmenger, Polarization Dynamics of VDF-TrFE Copolymers, IEEE Trans. Electr. Insul. 26 (1) (1991) 69–77, https://doi.org/10.1109/14.68230.

[23] M. Serridge, T.R. Licht, Piezoelectric Accelerometers and Vibration Preamplifiers: Theory and Application Handbook, Bruel & Kjaer (1987).

[24] D.P. Skinner, R.E. Newnham, L.E. Cross, Flexible composite transducers, Mater. Res. Bull. 13 (6) (1978) 599–607.

[25] R.E. Newnham, D.P. Skinner, L.E. Cross, Connectivity and piezoelectric-pyroelectric composites, Mater. Res. Bull. 13 (5) (1978) 525–536.

[26] H. Zarei, T. Brugo, J. Belcari, H. Bisadi, G. Minak, A. Zucchelli, Low velocity impact damage assessment of GLARE fiber-metal laminates interleaved by Nylon 6,6 nanofiber mats, Compos. Struct. 167 (2017) 123–131, https://doi.org/10.1016/j.compstruct.2017.01.079.

[27] H. Naderiallaf, P. Seri, G.C. Montanari, Designing a HVDC Insulation System to Endure Electrical and Thermal Stresses under Operation. Part I: Partial Discharge Magnitude and Repetition Rate during Transients and in DC Steady State, IEEE Access 9 (2021) 35730–35739, https://doi.org/10.1109/ACCESS.2021.3062440.

[28] G. Selleri, M.E. Gino, L. Gasperini, M. Zanoni, C. Gualandi, M.L. Focarete, D. Fabiani, Study on the polarization process for piezoelectric nanofibrous layers, IEEE Conference on Electrical Insulation and Dielectric Phenomena (2021).

[29] H. Naderiallaf, P. Seri, G. Montanari, On the calculation of the dielectric time constant of DC insulators containing cavities, IEEE Conference on Electrical Insulation and Dielectric Phenomena (2021).

[30] F.H. Kreuger, Industrial High DC Voltage: 1. Fields 2, Breakdowns 3.Tests. (1995).

[31] S. Abrate, Impact on Composite Structures, Cambridge University Press, 2005.